High Spatial Resolution Tomo-PIV of the Trachea Focussing on the Physiological Breathing Cycle

Sandra Melina Tauwald[1,2(✉)], Maurizio Quadrio[3], Markus Rütten[4], Christian Stemmer[5], and Lars Krenkel[1,2]

[1] Regensburg Center of Biomedical Engineering (RCBE), OTH and University of Regensburg, and Regensburg Center of Health Sciences and Technology (RCHST), Galgenbergstraße 30, 93053 Regensburg, Germany
melina.tauwald@oth-regensburg.de
[2] Department of Biofluid Mechanics, Technical University of Applied Sciences (OTH) Regensburg, Galgenbergstr. 30, 93053 Regensburg, Germany
[3] Department Aerospace Science and Technology, Politecnico Milano, Via Privata Giuseppe La Masa 34, 20156 Milan, Italy
[4] German Aerospace Center (DLR), Bunsenstr. 10, 37073 Göttingen, Germany
[5] Technical University of Munich (TUM), Chair of Aerodynamics and Fluid Mechanics, Boltzmannstr. 15, 85748 Munich, Germany
http://bfm.rcbe.de

Abstract. Investigations of complex patient-specific flow in the nasopharynx requires high resolution numerical calculations validated by reliable experiments. When building the validation base and the benchmark of computational fluid dynamics, an experimental setup of the nasal airways was developed. The applied optical measurement technique of tomo-PIV supplies information on the governing flow field in three dimensions. This paper presents tomo-PIV measurements of the highly complex patient-specific geometry of the human trachea. A computer-tomographic scan of a person's head builds the basis of the experimental silicone model of the nasal airways. An optimised approach for precise refractive index matching avoids optical distortions even in highly complex non-free-of-sight 3D geometries. A linear-motor-driven pump generates breathing scenarios, based on measured breathing cycles. Adjusting of the CCD cameras' double-frame-rate PIV-Δ t enables the detailed analysis of flow structures during different cycle phases. Merging regions of interest enables high spatial resolution acquisition of the flow field.

Keywords: Tomographic PIV · Flow visualisation · Breathing cycle · Nasal airflow

1 Introduction

The main component of the upper airways, the nasopharynx, is a key element in the breathing apparatus [1]. While its major function is to condition the inhaled

A. Dillmann et al. (Eds.): STAB/DGLR Symposium 2022, NNFM 154, pp. 569–578, 2024.
https://doi.org/10.1007/978-3-031-40482-5_54

air, the nasopharynx influences the whole breathing cycle [2,3]. According to various medical studies, nasal breathing difficulties affect tens of millions of people, resulting in public health costs of up to a billion euros annually [4]. To reduce the booming costs and maximise the rate of satisfactory results following surgery, surgeons require a system of indicators to support them in selecting the appropriate treatment [5]. With regard to respiration, computational methods offer great promise [6,7]. Examining the anatomical shape and physiological function of the upper airways from a fluid mechanical point of view considerably improve diagnostic precision while also minimising the number of surgery failures [4,7,8]. Such investigations are challenging, largely due to the complex flow characteristics created by the manifold structures of the inter- and intra-individual variations in geometry [6,9,10].The literature contains extensive information regarding ways of predicting nasal flow patterns by Computational Fluid Dynamics (CFD) and optical measurements [11]. CFD enables the analysis of patient-specific geometries based on CT scans. However, the lack of information complicates the choice of a suitable calculation model. Experimental studies are therefore indispensable for assessing a calculation's meaningfulness. Studies assessing experimental investigations are mainly based on the optical method of Particle Image Velocimetry (PIV) [4,12,13]. These investigations were primarily conducted on nose similar geometries and/or analysed with planar or stereoscopic (stereo)-PIV. One disadvantage of these methods is a loss accuracy, especially for thin volumes and turbulent flows [14]. Data on realistic nose models, investigated by tomographic (tomo)-PIV, remains very rare - mainly due to the complexity of the geometry and the challenging experimental setup. Since tomo-PIV considers voxels (vox) as uniform cubes in all dimensions, in-plane and cross-plane properties can be analysed. Tomo-PIV enables all three components of velocity to be analysed. A cyclic respiratory flow and a physiological geometry of the upper airways is assumed in experimental investigations in order to create the appropriate physiological conditions. Since tomo-PIV calculates the velocity field based on the particle shift between consecutive images, the timing of PIV components needs to be adjusted based on the breathing cycle phase. The presend paper uses tomo-PIV to present a method of analysing the three-dimensional velocity vectors and the vorticity in a patient-specific model of the nasopharynx while setting a boundary condition based on the physiological breathing cycle [5,11].

2 Methods

2.1 Development of the Phantom Model

The basis of the workflow was a clinical computer-tomographic (CT) scan of a person's head presenting a normal sino- nasal anatomy (approved by the Institutional Review Board of the San Paolo Hospital) (Fig. 1a). The CT scan was used to build a rapid-prototyped core representing the airway-part of the phantom model. To enable investigation of the smallest cavities of the upper airways in a sufficient resolution it was necessary to upscale (magnification factor M = 2)

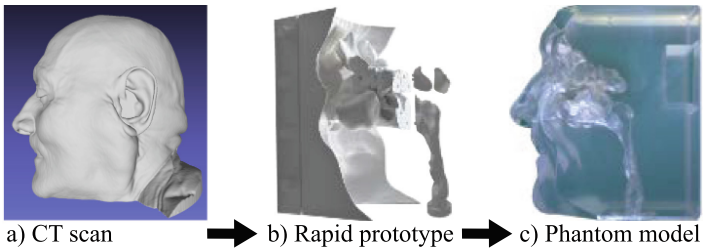

Fig. 1. Workflow of manufacturing the phantom model a) the initial CT scan, b) the scan-based water soluble rapid prototype and c) the final phantom model.

of the geometry. The rapid-prototyped airway model was made from calcium sulphate and a water-soluble binder (zp 131 powder/ zb 60 binder, Z Corporation, Burlington, USA) printed with ZPrinter 660Pro (3D Systems, South Carolina, USA) (Fig. 1b). Since rapid-prototyped models suffer from aliasing-effects, the 3D print was coated with 20 layers (final thickness of 0.15 mm) of a 2.5 wt/vol % polyvinylalcohol-distilled water solution (VWR chemicals, Pennsylvania, USA) for smoothing the surface. Fluorescence particles (Polysterol, Diameter 793 µm, ex/em = 530/607 nm, microparticles GmbH, Berlin, Germany) were then attached at defined locations of the model. These marker particles allow for precise local matching of the (subsequently calculated) velocity field and the stereolithography (STL) data of the rapid prototype using the software CADfix® (ITI, Milford, OH, US). For this alignment, a micro-CT scan of the rapid prototype was prepared and post-processed using the software Volume Graphics Studio (Volume Graphics, Heidelberg, Germany) and Netfabb® (Autodesk, Inc., San Rafael, CA, US). Then, the airway model was placed in an outer cast. As a final step, the mold was slowly filled with PDMS (Sylgard 184, Dow Corning, Michigan, USA). The model was cured under 2.5 bar pressure and 60° C in an autoclave. Finally, the airway-core was dissolved by repeated rinsing with water and subsequently cleaning with citric acid (Fig. 1c).

2.2 Experimental Setup

Tomo-PIV. Figure 2 shows the experimental tomo-PIV setup. It consists of a tomo-PIV system comprising three cameras, each fitted with CCD sensors (Imager Pro X 10, 1600×1200 pixel, LaVision GmbH, Göttingen, Germany), which is controlled centrally by a programmable timing unit (PTU). The PTU receives a TTL signal from the control unit of the linear-motor-driven piston pump (LinMot GmbH, Essen, Germany). The cameras were fitted with macro objectives (ZEISS, Milvus 2/135), Scheimpflug adapters, and cut-off filters. The light source used was a double pulsed Nd:YAG laser (EverGreen200 70–200 mJ @ 532 nm, 15 Hz, Lumibird, France) equipped with optical components. Knife edges were used to cut the diverging volume illumination into a RoI (region of interest) fitting volume. The RoI's volume was defined by the initial scale of the cameras' field of views (FoV)s and the depth of field (DoF) (50.5 mm × 34 mm × 17 mm). The geometry was mounted on a 3-axis traversing unit (isel Germany AG,

Eichenzell, Germany) and placed in a 800 L fish tank containing three portholes for the cameras at angles of 60° to each other. The fish tank was then filled with the working fluid (WF) (water-glycerol solution). The flow is induced at the trachea and exits the geometry at the nostrils. The tracer particles (PMMA-RhB, 20–50 µm, abs/emm = 560/584 nm, LaVision GmbH) exhibit a density ρ_{TP} of 1.19 g/ccm. The density of the WF $\rho_{WF} = 1.152\,g/cm^3$ was analysed by a pycnometer (DMA 35, Anton Paar GmbH, Osftildern, Germany). Particles with WF were premixed and injected into the flow with a syringe. The dynamic viscosity of the WF μ_{WF} was investigated using a rotational rheometer with a cylinder geometry (Discovery HR20, TA Instruments, New Castle, Delaware, USA). μ_{WF} was measured by conducting a flow-sweep test within shear rates of between 10^{-1} to 10^2 1/s.

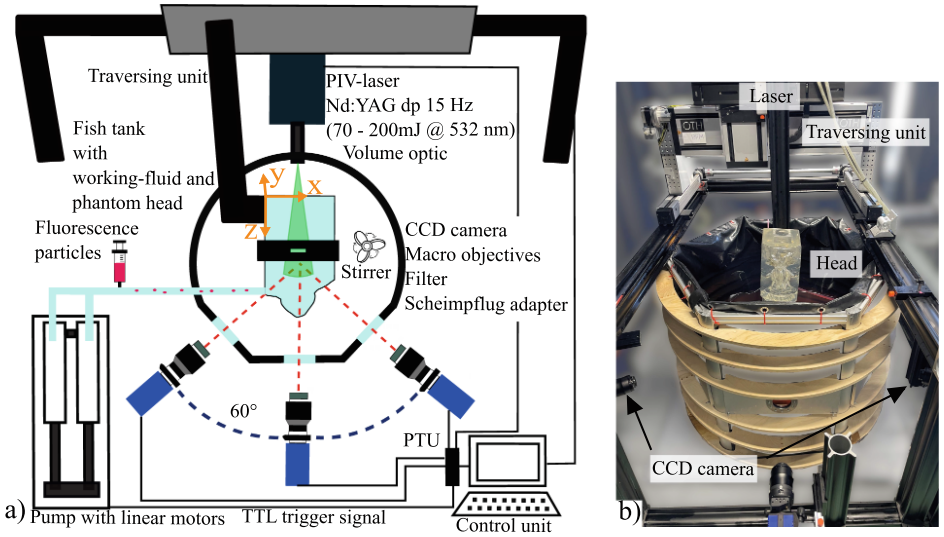

Fig. 2. Setup showing the main tomo-PIV components. Fig. 2a) shows a schematic view comprising three CCD cameras equipped with Scheimpflug adapters, macro objectives and filters positioned at 60° angles. The phantom head is placed in a fish tank filled with WF by a traversing unit. The flow is induced by a linear-motor-driven piston pump. Induced tracer particles are illuminated by a laser. All components are controlled centrally by a PTU. Fig. 2b) shows a photography of the setup.

Refractive Index Matching (RIM). To achieve an optimised match of the refractive indices (RI) between the WF (water-glycerol-mixture) and the PDMS head, an in-site method was developed. The method enables avoiding inaccuracies introduced by the refractometer measuring RI of solids (ORM 1RS, KERN & SOHN GmbH, Balingen, Germany). A light sheet from a continuous line laser (Ray Power 450 DPSS, Dantec Dynamics GmbH, Ulm, Germany) enters the fish tank through one of the portholes, is deflected by a mirror, and detected on it exiting the fish tank through the 120° angled porthole. The light sheet exiting the fish tank is visualised on scaled paper and captured by a camera (D3400, Nikon Corporation, Tokyo, Japan) fitted with a magnifying objective (AF-P DX

NIKKOR, 22/18, Nikon Corporation, Tokyo, Japan). A reference image of the light sheet was captured without crossing the model and images were captured while the phantom head was placed in the laser-line. The RI of the WF was adopted while adding specific amounts of water/glycerol and measured by a digital refractometer.

Linear-Motor-Driven Piston Pump. Flow rates were induced by a pump containing two linear motors and two pistons (diameter $\varnothing_{\text{pump}} = 50\,\text{mm}$, driving length $l_{\text{pump}} = 170\,\text{mm}$), driven by a programmable logic controller (PLC) and controlled by Twincat software (Beckhoff Automation GmbH, Verl, Germany). To investigate the flow field by a constant speed of the pump's pistons, the speed of a single piston was set to 0.03 m/s forwards/backwards (cycle length 9.2 s), resulting in a flow rate of 130 ml/s with both pistons. To induce a physiological flow cycle, 30 cycles of a healthy subject were captured by a spirometer (Pneumotrac$^{\text{TM}}$, Vitalograph® GmbH, Hamburg, Germany) and processed by the proprietary Spirotrac 6 software. The cycles were processed using Matlab software (Matlab® R2020b, Mathworks Inc., MA, US) applying dynamic time-warping and fitted by a 7$^{\text{th}}$ degree polynomial function. The captured flow rate Q_{vivo} was adjusted to the experimental conditions Q_{vitro} using Reynolds' similarity [4].

$$Q_{\text{vitro}} = Q_{\text{vivo}} * M * \frac{\nu_{\text{vitro}}}{\nu_{\text{vivo}}} \tag{1}$$

2.3 Tomo-PIV Measurements and Timing

All components of the tomo-PIV setup were controlled by DaVis software. The tomo-PIV's capturing was triggered by starting the pump cycle. The PIV's intra-doubleframe-rate (PIV-Δ t) was set to 700 µs during a constant flow rate for a particle shift of between 5 and 8 pixels (pix). During breathing flow rates, loops of PIV-Δ t ranging from 120 µs to 2120 µs with an increment step of 400 µs were analysed. The images with a suitable particle shift were then post-processed. The cameras were precalibrated by a plate calibration target and following by Volume Self Calibration (VSC) based on the post-processed particle images. For PIV-algorithm, the final window size was set to 64 vox, with a maximum expected displacement to 16 vox. Four different FoVs were captured by moving the phantom head through a distance of 10 mm on the z-axis and 20 mm on the x-axis. The flow fields were merged by calculating the arithmetic mean of the overlapping areas using Matlab.

3 Results

3.1 Refractive Index Matching

The components of the WF were water (RI water $\eta_{H_2O} = 1.333$) and glycerol (RI glycerol $\eta_{\text{Glyc}} = 1.473$). The light sheet's reference projection, without crossing

the phantom head, displays a straight, uninterrupted line, as shown in Fig. 3, while the projection of the line crossing the phantom head at an RI of $\eta_{WF} = 1.4142$ displays kinks. Adding water down to $\eta_{WF} = 1.4138$, again results in a continuous projection of the line.

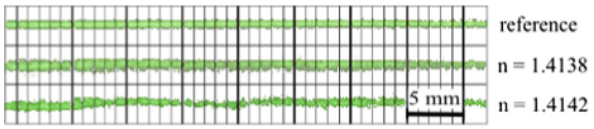

Fig. 3. Results of RIM of the WF and phantom head, reference image of the projected light sheet without passing the geometry (top), best matching RI (middle) and kinked light sheet caused by different RIs (bottom).

3.2 Positioning and Merging of RoIs

The final resolution achieved was 32 pix/mm. The DoF of the cameras was 17 mm. The reconstruction and vector calculation were performed for the whole volume of the FoV, while the vector fields were subsequently cropped to a volume of 45 mm × 33 mm × 17 mm. To increase the RoI, vector fields are measured in four different positions and were merged afterwards. Moving the traversing unit trough 10 mm in the z-dimension led to an overlap of 42 % of the RoIs, while a movement through 20 mm in the x-dimension led to an overlap of 28 %. Marker particles were used to combine the vector field's coordinate system with that of the scan. Fig. 4 shows the merging process of the four measurement positions (RoI1-4, Fig. 4 corners). For illustrating the high-resolution within the boundary layer regions, isosurfaces of each RoI with a low velocity magnitude ($|V| = 0.124$ m/s) are shown. RoI1 indicates the reference position, while RoI2 was moved along the z-axis, RoI3 along the z-axis and x-axis and RoI4 along the x-axis. Merging RoI1-4 resulted in a RoI's volume of 70.18 mm × 32.79 mm × 26.35 mm (Fig. 4 centre). The smallest cavity of the geometry, located at the ethmoidal sinuses, comprises a cross sectional area of 4 mm^2, which can be investigated with the spatial resolution of 32 pix/mm thus resulting in $4 * 10^3$ pix for this area. The investigated RoI reaches 60 cm^3 and therefore $2 * 10^9$ vox.

3.3 Measurements of Cyclic Flow Rates

The overall cycle had a duration of 3.59 s. The transition point from inhalation to exhalation was located at 1.97 s. The measurements of the dynamic viscosity of the WF resulted in $\mu_{WF} = 9.27$ mPas, the density measurements of the WF yielded a value of $\rho_{WF} = 1.152$ g/cm^3 and thus brings with it a difference to the density of the tracer particles $\rho_{TP} - \rho_{WF}$ of 0.04 g/cm^3. Including the enlargement (M = 2), the ratio of flow rates results a value of $Q_{vitro}/Q_{vivo} = 0.94$. Since cyclic breathing results in time varying flow rates, an adaption of the

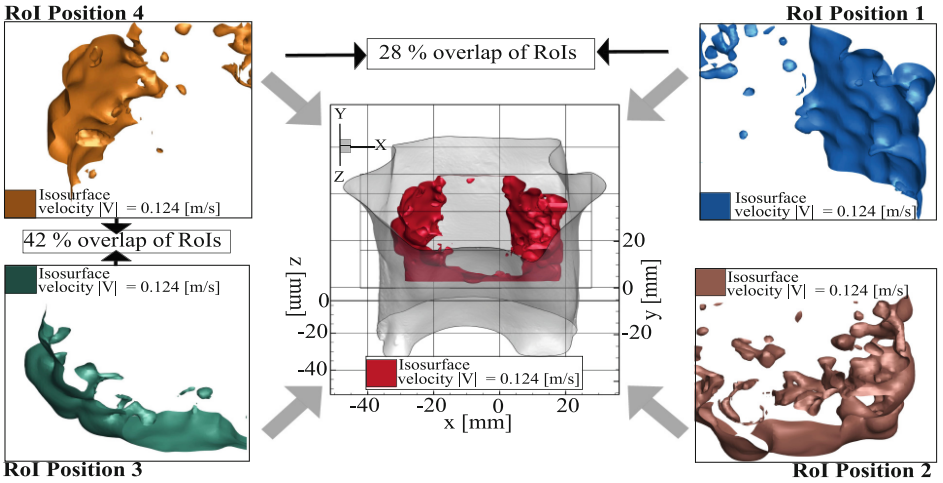

Fig. 4. Visualisation of the combining process of four RoIs. Isosurfaces at a velocity magnitude of $|V| = 0.124\,\mathrm{m/s}$ of the ROIs for positions 1–4 are shown at the corners, coded in different colours. The centre shows the isosurfaces for the combination of the four RoIs after calculation of the arithmetic mean in the overlapping areas at the same velocity magnitude.

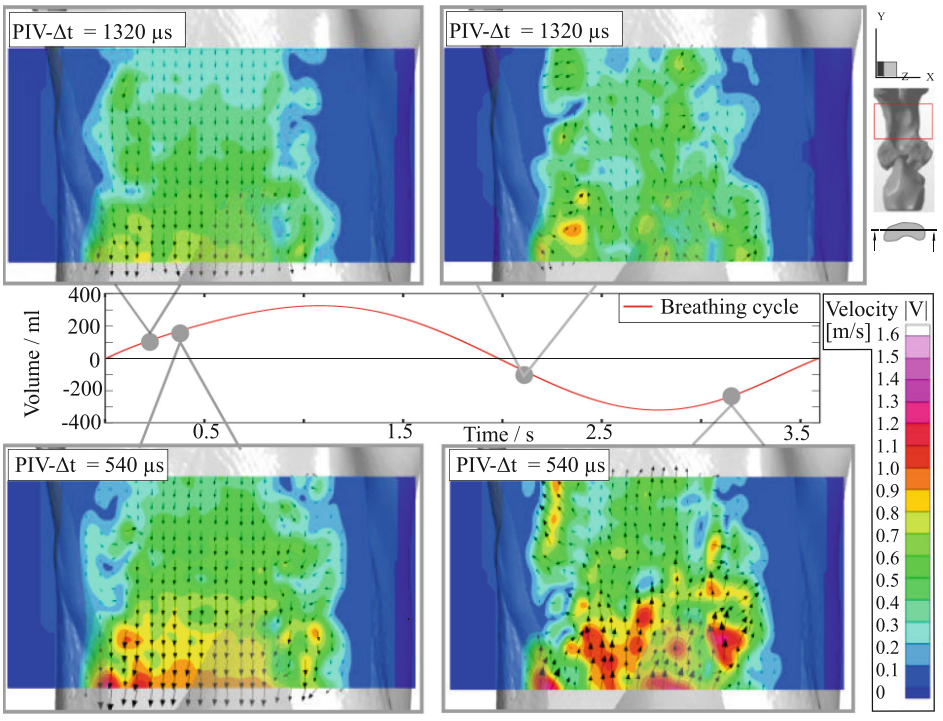

Fig. 5. Snapshots of four breathing cycle phases. Representative velocity profiles at cycle phase 0.045, 0.29, 2.21 and 3.17 s are shown colour-coded. The lengths of the projected vectors is relative to their velocity magnitude.

PIV-Δ t between different phases was necessary. This is shown on exemplary cycle phases at 0.29 s and 2.21 s for a PIV-Δ t of 1320 µs, cycle phases at 0.045 and 3.17 s showed a suitable particle shift for PIV-Δ t of 520 µs. Figure 5 shows four snapshots of the flow. An example slice is visible at z-position –

0.49 mm, where the volume consists of RoI1 and RoI2 with an overlap of 28 %. The velocity magnitude is shown colour-coded and velocity components are visualised by vectors. The lengths of the vectors are relative to their velocity magnitude. A decreasing velocity while reaching the boundaries of the geometry can be seen in Fig. 5. The vector projections indicate a main flow direction that depends on the inhalation or exhalation phase within the breathing cycle. The cycle phase at 0.29 s with a pump flow rate of 130 ml/s shows a velocity magnitude of up to 0.7 ms in the region where the inner diameter of the geometry decreases. Velocities range from 0 to 1.6 m/s, depending on the cycle phase. As shown in Fig. 5, the inhalation velocity fields display smoother gradients than the exhalation fields. The cycle phase at 2.21 s displays a peak in the lower left corner, while the cycle phase at 3.17 displays several peaks spread throughout the entire investigated volume. A difference in speed at the upper and lower edges of the RoI is noticeable. This can be explained by the reducing cross-sectional area of the trachea at RoI's location. A difference in speed at the upper and lower edges of the RoI is noticeable. This can be explained by the reducing cross-sectional area of the trachea at RoI's location. A difference between inhalation and exhalation flow profiles in Fig. 5. is visible. The smoothness of the flow profile during the inhalation in comparison to the exhalation may be due to the position of the pump connector as well as the geometry itself. The flow is conditioned by almost the entire geometry during inhalation at the investigated RoI in the trachea. Whereas in case of the exhalation, the flow is analysed right after exiting the connector of the pump after passing the complex geometrical part of the pharyngeal tonsils. The tonsils show two significant protrusions directly in front of the RoI. In order to make a statement about the flow profiles, optimisation with regard to the flow inducing position is necessary. Additionally, the different flow patterns between inhalation and exhalation underline the need of an analysis of the entire geometry.

3.4 Comparison Constant and Cyclic Flow Rate

Since a flow rate of 130 ml/s was induced during investigations of the constant flow cycle and breathing cycle phase at 0.045 s, the velocity profiles were compared. Figure 6 shows isosurfaces (Fig. 6 left) for the velocity magnitudes $|V| = 0.56$ m/s and 0.11 m/s. The right-hand side of Fig. 6 shows the velocity magnitude of a representative z-slice, colour-coded. The length of the visualised vectors is relative to their velocity magnitude. The upper part shows the results for constant flow, the lower part for the breathing cycle. While the isosurfaces are similar in the x-dimension at a velocity magnitude of 0.11 m/s, the isosurfaces for a velocity magnitude of 0.56 m/s occupy a larger area for the constant flow. The same applies to the visualisation on the representative z-slice. Vector projections show for both investigations a main direction in decreasing y-dimension. While comparing the flow profile of the constant flow rate and the cyclic flow rate, similarities are noticeable with regard to the direction of the flow, but there are differences in the velocity magnitude. Cyclic flow rates can induce additional transient effects, that might not occur in a steady flow rate boundary condition.

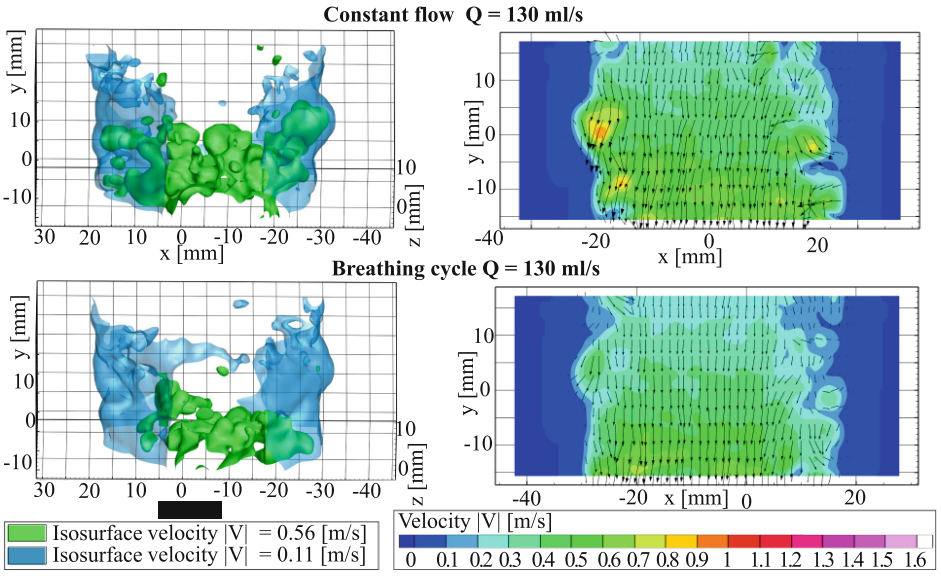

Fig. 6. Comparison of the constant flow rate Q = 130 ml/s and the same flow rate during the breathing cycle.

Since flow cycles in this study are not adapted by Womersley similarity, the high density of the working fluid in comparison to air, can enhance the differences due to the fluids intertia.

4 Conclusion

The resolution of 32 pix/mm and the two-fold magnification of the geometry enable an accurate analysis of smaller flow structures. The new RIM method, integrated in the setup, minimizes the errors caused by optical distortion, leading to a satisfactory VSC. The linear-motor-driven pump provides a suitable method for inducing a physiological breathing cycle. Nevertheless, since the present investigation is based on data from a single test-person, larger studies with several test-persons are essential in order to obtain a representative breathing cycle. The output trigger of the pump's control unit proved to be a suitable signal for activating image capturing in an investigation of several cycle phases. The micro-CT scan of the rapid prototype enables precise realignment of the experimental data, since marker particles are visible both in the final data and in the captured images. The traversing unit has the advantage of creating traceable locations for the experimental results relative to the geometry. Results can be merged by calculating an arithmetic mean for the overlapping areas. However, since the arithmetic mean was investigated on single snapshots of the flow, statistical surveys to determine standard deviations of the velocity profiles in the overlapping areas are needed. As shown in Fig. 5, adjusting the PIV-Δ t enables the investigation of velocity fields with different velocity magnitudes, caused by the breathing-cycle-dependent flow rate. To prove this requires multiple repeat measurements. The described methods were applied to an example position of

the phantom head with a flow rate derived from a representative breathing cycle. Investigations on the whole flow field as a whole requires parametric studies to determine a suitable overlap of RoIs and averaging of overlapping flow parts. Additionally, since breathing is a repeating cycle, measurements under identical conditions over several cycles are necessary to analyse the development of flow over time.

Acknowledgements. This work is supported by the RCHST, the RCBE, and the Bavarian Academic Forum (BayWISS). Special thanks to Florian Erzinger for his support in the implementation of the experiments. Further thanks go to our colleagues of the project OpenNOSE for the intensive interdisciplinary exchange and the active support.

References

1. Morris, R.: Functional anatomy of the upper airway. Emerg. Med. Clin. North. Am. **6**, 639–669 (1988)
2. Kanda, A., Kobayashi, Y., Asako, M., Tomoda, K., Kawauchi, H., Iwai, H.: Regulation of interaction between the upper and lower airways in united airway disease. Med. Sci. (Basel) **7**(2), 27 (2019)
3. Licari, A., Castagnoli, R., Denicolo, C.F., Rossini, L., Marseglia, A., Marseglia, G.: The nose and the lung: united airway disease? Front. Pediatr. **5**, 44 (2017)
4. Cozzi, F., Felisati, G., Quadrio, M.: Velocity measurements in nasal cavities by means of stereoscopic piv - preliminary tests. In: Journal of Physics: Conference Series, vol. 882, p. 012010 (2017)
5. Quadrio, M., et al.: Review of computational fluid dynamics in the assessment of nasal air flow and analysis of its limitations. Eur. Arch. Othrhinolaryngol. **271**, 2349–2354 (2014)
6. Lynch, K.P., Scarano, F.: Experimental determination of thomographic piv accuracy by a 12-camera system. Meas. Sci. Technol. **25**, 1–10 (2014)
7. Lintermann, A., Schröder, W.: A hierarchical numerical journey trough the nasal cavity: from nose-like models to real anatomies. Flow Turbul. Combust. **102**, 89–116 (2019)
8. Naftali, S., Rosenfeld, M., Wold, M., Elad, D.: The air-conditioning capacity of the human nose. Ann. Biomed. Eng. **33**, 545–553 (2005)
9. Gambaruto, A.M., Taylor, D.J., Doorly, D.J.: Decompostition and description of the nasal cavity form. Ann. Biomed. Eng. **40**, 1142–1159 (2012)
10. Elad, D., Naftali, S., Rosenfeld, M., Wolf, M.: Physical stresses at the air-wall interface of the human nasal cavity during breathing. J. Appl. Physiol. **100**, 1003–1010 (2005)
11. Hörschler, I., Schröder, W., Meinke, M.: On the assumption of steadiness of nasal cavity flow. J. Biomech. **43**, 1081–1085 (2010)
12. Hopkins, L.M., Kelly, J.T., Wexler, A.S., Prasad, A.K.: Particle image velocimetry measurements in complex geometries. Exp. Fluids **29**, 91–95 (2000)
13. Spence, C.J.T., Buchmann, N.A., Jermy, M.C.: Unsteady flow in the nasal cavity with high flow therapy measured by steroscopic piv. Exp. Fluids **52**, 569–579 (2012)
14. Michaelis, D., Wieneke, B.: Comparison between tomographic piv and stereo piv. In: International Symposium of Laser Techniques to Fluid Mechanics (2008)